

# Entry Configurations and Performance Comparisons for the Mars Smart Lander

Mary Kae Lockwood\* and Richard W. Powell†

NASA Langley Research Center, Hampton, Virginia 23681

Kenneth Sutton‡

National Institute of Aerospace, Hampton, Virginia 23666

Ramadas K. Prabhu§

Lockheed Martin Engineering and Sciences Company, Hampton, Virginia 23681

and

Claude A. Graves,¶ Chirold D. Epp,\*\* and Gilbert L. Carman††

NASA Johnson Space Center, Houston, Texas 77058

The Mars Smart Lander (MSL, renamed and redefined as the Mars Science Laboratory) will provide scientists with access to previously unachievable landing sites by providing precision landing to less than 10 km of a target landing site with landing altitude capability to 2.5 km above the Mars Orbiter Laser Altimeter geoid. Precision landing is achieved by using the aerodynamic forces on the entry body to aeromaneuver through the Martian atmosphere during the entry phase of flight. The entry body is designed to provide aerodynamic lift. The direction of the aerodynamic lift vector, defined by the vehicle bank angle, is commanded by the onboard entry guidance, to converge downrange and crossrange errors by parachute deploy, while meeting the parachute deploy constraints. Several approaches and entry body configurations for providing aerodynamic lift can be considered, including axisymmetric capsule configurations with offset c.g.s using ballast or packaging, aerodynamically shaped capsule-type configurations, and alternate configurations such as mid-lift-to-drag-ratio vehicles. The design considerations, entry configurations, and entry performance of the Mars Smart Lander are described.

## Nomenclature

$C_A$	=	axial-force coefficient (axial force/ $qS$ )
$C_D$	=	drag coefficient (drag/ $qS$ )
$C_L$	=	lift coefficient (lift/ $qS$ )
$C_m$	=	pitching-moment coefficient (pitching moment/ $qSl$ )
$C_{m\alpha}$	=	$\delta C_m / \delta \alpha$ , $\text{deg}^{-1}$
$C_N$	=	normal-force coefficient (normal force/ $qS$ )
$C_{n\beta\text{dyn}}$	=	$C_n$ beta dynamic
$D$	=	sensed drag, N
$D_{\text{ref}}$	=	reference drag, N
$g$	=	acceleration caused by gravity, $\text{m/s}^2$
$h$	=	altitude, m
$l$	=	reference length, m
$M$	=	freestream Mach number
$m, M$	=	mass, kg
$q$	=	dynamic pressure, Pa

$R$	=	great circle range to target, km
$r$	=	magnitude of radius vector from Mars center to spacecraft, km
$r_e$	=	Mars equatorial radius, m
$S$	=	reference area, $\text{m}^2$
$T_0$	=	freestream temperature
$t$	=	time, s
$V, v$	=	relative velocity magnitude, $\text{m/s}$
$V_0$	=	freestream velocity
$X_{\text{cg}}$	=	axial c.g. location, m
$Y_{\text{cg}}$	=	lateral c.g. location, m
$Z_{\text{cg}}$	=	vertical c.g. location, m
$\alpha$	=	trim angle of attack, $\text{deg}$
$\beta_m$	=	ballistic coefficient ( $M/C_D S$ ), $\text{kg/m}^2$
$\gamma$	=	relative flight-path angle, $\text{deg}$
$\rho, \rho_0$	=	freestream density, $\text{kg/m}^3$

## I. Introduction

THE Mars Smart Lander (MSL) entry capsule is designed to accommodate potentially large science payloads of 300 kg or more while providing the capability for precision landing, with landing accuracies of  $\pm 10$  km (99.7 percentile) from a designated target site and at altitudes of 2.5 km or less above the Mars Orbiter Laser Altimeter (MOLA) geoid. Figure 1 shows a Mars Smart Lander (MSL) concept packaged with a large rover and a pallet lander. The heat shield shown is the axisymmetric 70-deg sphere cone similar to Viking, Pathfinder, and Mars Exploration Rover. The biconic back-shell for MSL is used to obtain a large payload volume and high volumetric efficiency in payload packaging.

To achieve a precision landing, aeromaneuvering must be employed during the hypersonic entry to converge the range errors caused by delivery state errors and variations in atmospheric density and vehicle aerodynamic characteristics. The MSL is designed to trim at an angle of attack, as shown in Fig. 2, producing aerodynamic lift. The MSL entry guidance commands the vehicle bank angle, controlling the direction of the lift vector, enabling control of the vehicle downrange and cross range for delivery to the

Received 4 February 2003; revision received 5 July 2005; accepted for publication 5 July 2005. This material is declared a work of the U.S. Government and is not subject to copyright protection in the United States. Copies of this paper may be made for personal or internal use, on condition that the copier pay the \$10.00 per-copy fee to the Copyright Clearance Center, Inc., 222 Rosewood Drive, Danvers, MA 01923; include the code 0022-4650/06 \$10.00 in correspondence with the CCC.

\*Aerospace Engineer, Mail Stop 489, Exploration Systems Engineering Branch. Member AIAA.

†Aerospace Engineer, ST, Mail Stop 489, Exploration Systems Engineering Branch. Associate Fellow AIAA.

‡Senior Research Fellow, Mail Stop 408A, National Institute of Aerospace. Associate Fellow AIAA.

§Senior Aerospace Engineer, Mail Stop 408A, Lockheed Martin Space Operations, Langley Program Office.

¶Senior Technical Advisor, Mail Stop EX, Explorations Systems Engineering Division. Associate Fellow AIAA.

\*\*Senior Aerospace Engineer, Mail Stop EX, Exploration Systems Engineering Division. Member AIAA.

††Aerospace Engineer, Mail Stop DM42, AST Data Systems, Flight Design and Dynamics Division.

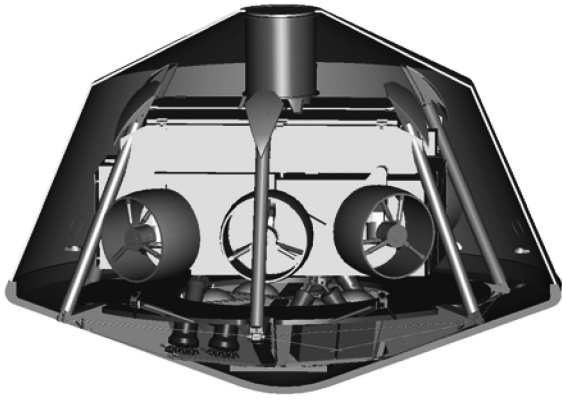


Fig. 1 Mars Smart Lander concept.

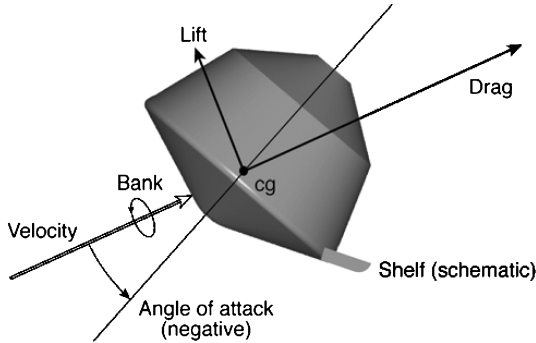


Fig. 2 Entry body lift, drag, and bank.

parachute deploy terminal point. The entry guidance to be used for MSL is a derivative of the Apollo entry guidance approach<sup>1</sup> and has been tested extensively in high-fidelity simulations for use at Mars,<sup>2</sup> including the MSL Program to Optimize Simulated Trajectories simulation.<sup>3</sup>

## II. Vehicle Design Parameters for Effective Aeromaneuvering

To successfully steer the trajectory to the desired terminal point conditions at parachute deployment, the vehicle must be designed to provide sufficient control authority. The planar equations of motion for atmospheric flight can be expressed as

$$\frac{dV}{dt} = -\left(\frac{\rho}{2\beta_m}\right)V^2 - g \sin(\gamma) \quad (1)$$

$$V \frac{d\gamma}{dt} = \left(\frac{\rho}{2\beta_m}\right)V^2 \left(\frac{C_L}{C_D}\right) - \cos(\gamma) \left(g - \frac{V^2}{R_e + h}\right) \quad (2)$$

where the subscript  $V$  refers to the vertical component of  $C_L/C_D$ . This ballistic coefficient is defined as the mass cross-sectional density of the vehicle divided by the drag coefficient:

$$\beta_m = m/C_D S \quad (3)$$

### A. Lift-to-Drag Ratio

The primary contributor to entry range dispersion for Mars Smart Lander is the delivery error in the flight-path angle at entry interface. An error in the initial flight-path angle results in a diverging range error with respect to the nominal reference trajectory profile. This range error will continue to increase until sufficient atmospheric density has been encountered to provide effective flight-path-angle control. Targeting for a steeper nominal entry flight-path angle will result in smaller range errors, but will also result in larger vehicle load factors and less available flight time to converge the range errors. For the Mars Smart Lander direct entry conditions in the 2009

opportunity, a flight-path angle of approximately  $-14.5^\circ$  at entry interface provides the best compromise between these effects. As can be seen in Eq. (2), the rate of change of flight-path angle is directly proportional to the in-plane vertical component of lift-to-drag ratio ( $L/D$ ). The magnitude of the  $L/D$  required to achieve the target range is a function of the delivery error and the amount of flight time remaining, as well as the variations in vehicle  $L/D$  and atmospheric density. For a given worst-on-worst combination of the preceding dispersions, the vehicle trimmed lift coefficient can be scaled to determine the minimum required  $L/D$  that will provide sufficient control authority to achieve the target. The original  $L/D$  requirement for MSL was determined for the 2005 opportunity. To successfully achieve the desired terminal range in the presence of the  $\pm 0.6^\circ$  99.7% delivery flight-path-angle errors resulting from radiometric-only navigation for the 2005 opportunity and the landing location, a minimum nominal average  $L/D$  of 0.22–0.25 was required. As shown in Ref. 4, maximum range errors of approximately 110 km were converged, resulting in 99.45% of the cases with navigated distances from the target of 3 km. With improvements in the navigation system including delta differential one-way ranging and optical navigation, in addition to radiometric navigation, the delivery state dispersions for a 2009 arrival to the same target site were reduced to  $\pm 0.34^\circ$  deg 99.7%. Results for this design are shown later in this paper.

### B. Ballistic Coefficient

A vehicle design that provides an adequate  $L/D$  for trajectory range control will not necessarily achieve acceptable terminal conditions if the ballistic coefficient is not compatible with the parachute deployment constraints. As can be seen in Eq. (1), the deceleration caused by drag is larger for smaller ballistic coefficients. The atmospheric density required at terminal entry conditions to achieve a given velocity and drag acceleration at parachute deployment will increase in direct proportion to the ballistic coefficient. Therefore, either the parachute deployment speed (Mach number) must increase and/or the deployment altitude must decrease for vehicles with larger ballistic coefficients.

The parachutes currently in use by the Mars robotic lander program were certified to a deployment envelope based on the Viking lander design, which had a ballistic coefficient of approximately  $64 \text{ kg/m}^2$ . The Mars Pathfinder and MSP '01 lander designs had similar ballistic coefficients to Viking and were capable of achieving the required parachute deployment Mach number and dynamic pressure envelope at nominal altitudes of approximately 15–16 km. An early Mars Smart Lander baseline configuration has a ballistic coefficient of approximately  $114 \text{ kg/m}^2$  at parachute deployment. To maintain the deployment Mach number within the Viking envelope, the nominal altitude at deployment must necessarily decrease to approximately 10.5 km above the MOLA geoid. Dispersions in drag coefficient and atmospheric density result in a large variation in the deployment altitude. To preserve adequate time to accomplish a safe terminal deceleration and landing to a 2.5-km elevation site, a backup deployment command or override is issued. For the early MSL design in the 2005 opportunity, many cases were triggered by this backup deployment command, indicating that ballistic coefficients any larger than the baseline would result in a degradation in the range accuracy at deployment as a result of having no remaining margin from the parachute deployment constraints.

## III. Entry Body Configuration Design Requirements

To provide the necessary scontrol authority required to achieve precision landing and to meet the Viking parachute deployment qualification box, the entry body design requirement is to provide an  $L/D = 0.25$  and  $M/C_D S = 110 \text{ kg/m}^2$ . The entry body configuration must meet several additional requirements and objectives. The vehicle must fit within the maximum static payload diameter of 4.572 m for the Delta IV launch vehicle with a 5-m payload shroud shown in Fig. 3. The baseline concept load path at launch, with the lander attached to the cruise ring through the heat shield, must be maintained.

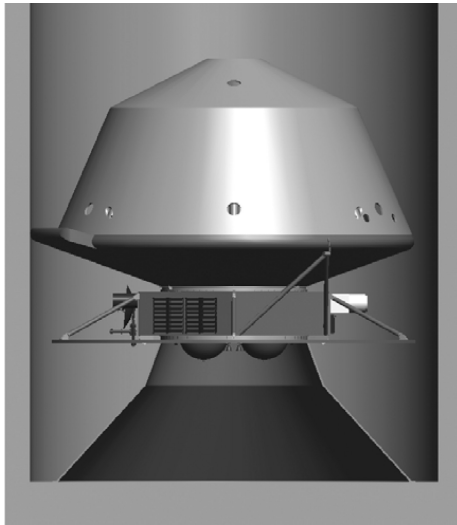


Fig. 3 MSR concept in Delta IV 5-m shroud.

Initially, the entry body design was designed to provide the required  $L/D$  with a minimum mass penalty for a given lander design and mass. The objective for the configuration trades was to achieve the  $L/D$  with less mass penalty than that for the ballasted radial center-of-gravity offset axisymmetric configuration. This requirement was later changed to support future design of a Mars Sample Return (MSR) lander. MSR requirements are to maintain the precision landing and therefore the  $L/D$  requirement of MSR. However, instead of minimizing the heat-shield mass for a given lander design, the requirement for MSR is to maximize the delivered mass to the surface of Mars. This requirement drives the vehicle design to the maximum cross-sectional area available in the launch vehicle, as well as maximum drag for the same  $L/D$ . Although much of the design space originally defined for MSR can be applied and evaluated against the new MSR-derived requirements, the change has a significant impact on the downselect criteria and on the design selected.

An additional design consideration for the entry body is the trim angle of attack of the entry body at supersonic parachute deploy. Viking qualified the magnitude of the angle of attack at parachute deploy to a maximum of 15 deg. For  $L/D = 0.25$  the trim angle of attack at parachute deploy exceeds 15 deg. It will be necessary to consider alternate approaches to meeting or modifying the angle-of-attack constraint while providing the control authority required. Alternatives include canting the parachute canister relative to the axis of symmetry of the entry body, using the reaction control system (RCS) to decrease the angle of attack at supersonic chute deploy, modifying the design to trim at lower angle of attack at parachute deploy and still achieve  $L/D = 0.25$  through most of the entry phase (although the benefit of higher  $L/D$  is reduced with this approach), completing enough testing and analysis to allow the angle of attack at parachute deploy to increase.

Another consideration in the design of the entry body configuration is a desire to minimize the sensitivity of the  $L/D$  and  $M/C_D S$  to axial c.g. location. Minimizing this minimizes the sensitivity of the entry body aerodynamic performance and heat-shield design to packaging through the design evolution and also minimizes the impact of mass uncertainties in the final design on flight performance. Although restrictions in axial c.g. movement are common constraints, the additional constraint resulting from the heat-shield shape might be an unnecessary added complexity and might reduce the robustness of the design.

Throughout the conceptual configuration design, the internal packaging was assumed to remain the same as the baseline. For the low  $L/D$  configurations, the backshell shape also remained the same as the baseline.

#### IV. Baseline Configuration

The baseline entry body concept is a 70-deg sphere-cone heat-shield configuration. It achieves the  $L/D$  by using ballast to provide

a radial c.g. offset, such that the entry vehicle trims at an angle of attack. The required radial c.g. offset and trim angle of attack to produce a given  $L/D$  for the baseline are shown in Table 1. (Axial force is the primary contributor to the lift vector; thus, flying at a negative angle of attack produces a positive lift.) To achieve the  $L/D = 0.25$  requirement, approximately 0.024 radial c.g. offset normalized to the maximum vehicle diameter is required. Also shown is the resultant coefficient of drag. Figures 4a–4c show the  $L/D$ ,  $C_D$ , and trim angle of attack as a function of flight velocity, and as a function

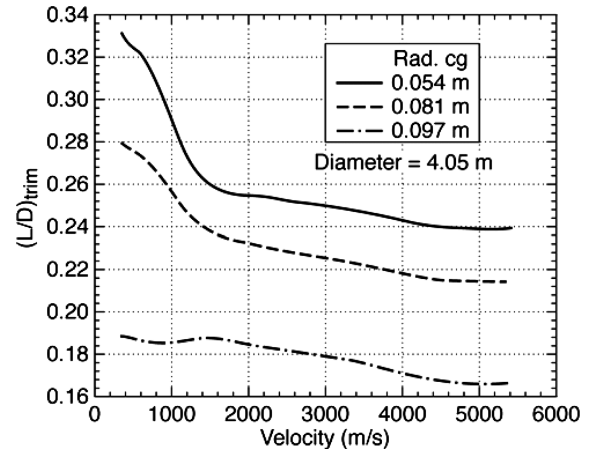


Fig. 4a Baseline vehicle  $L/D$  vs velocity along nominal trajectory.

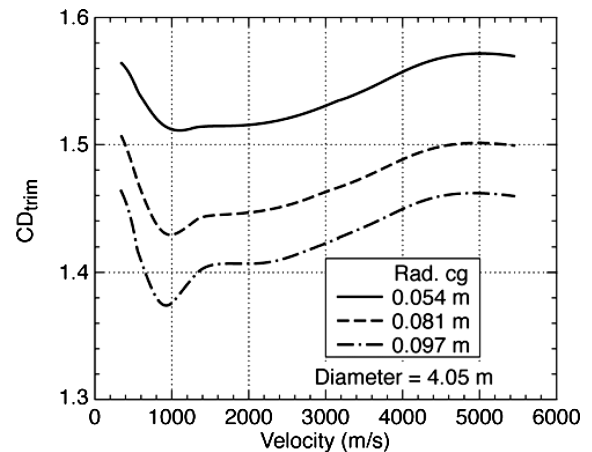


Fig. 4b Baseline vehicle drag coefficient vs velocity along nominal trajectory.

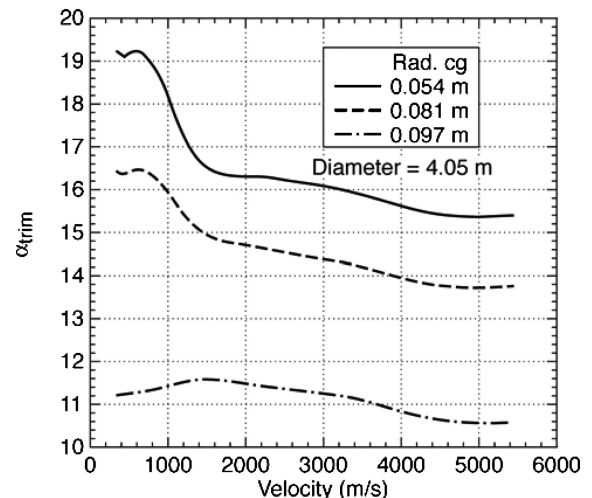


Fig. 4c Baseline vehicle trim angle of attack vs velocity along nominal trajectory.

of radial c.g. offset for the baseline. Note that Fig. 4c shows the nominal angle of attack at parachute deploy (at approximately 400 m/s) for the  $L/D = 0.25$  configuration to be greater than 15 deg. Currently the entry autopilot controller<sup>5</sup> is designed with a 2–3-deg deadband in angle of attack, to allow for uncertainties and perturbations, increasing the possible angle of attack at parachute deploy to 21–22 deg.

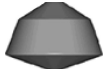
The ballast required to achieve the radial c.g. offset of the baseline configuration is significant resulting in either a large mass penalty to provide the  $L/D$  for a given lander or a large mass penalty on landed mass for the MSR lander requirement. Alternatives include providing the offset c.g. through packaging or defining an alternate entry body configuration to achieve performance similar to or better than the baseline with a significantly lower mass penalty. The alternate entry body configuration is the option discussed next.

## V. Entry Body Configurations

Figure 5 illustrates the representative design space considered for the MSL after an initial downselect. “Axisymmetric radial c.g. offset” and “tab/shelf” configurations compose a set of low  $L/D$  configurations considered. The ellipsed configuration was considered for the mid- $L/D$  class of configurations. These configurations will be described in further detail next.

Tab concepts were investigated as early as 1961 (Ref. 6) and considered again for the 2001 Mars Surveyor Program (MSP) Precision Lander mission.<sup>7</sup> An illustration of the parameters used to define a tab or shelf configuration is shown in Fig. 6. The MSP ’01 Lander

**Table 1** Baseline configuration hypersonic performance at Mach 24 as a function of radial c.g. offset

Baseline characteristic			
	$L/D = 0.17$	$L/D = 0.21$	$L/D = 0.24$
Alpha trim, deg	−10.6	−13.7	−15.4
c.g. rad/max. vehicle diam	0.013	0.020	0.024
$CD$	1.57	1.5	1.46

mission proposed using a single time-deployable tab to achieve the desired  $L/D$  for aeromaneuvering. The concept considered has a tab angled 90 deg to the axis of symmetry of the 70-deg sphere-cone heat shield and mounted behind the maximum diameter of the entry body to allow the tab to be mounted to the backshell of the MSP ’01 design. Three tab sizes, designated flap 1, flap 2, and flap 3, each with the same span but increasing in height, and therefore size, were tested in the Langley Research Center (LaRC) 20 Inch M6 CF4 tunnel for aerodynamic force and moment coefficients.<sup>7</sup> The

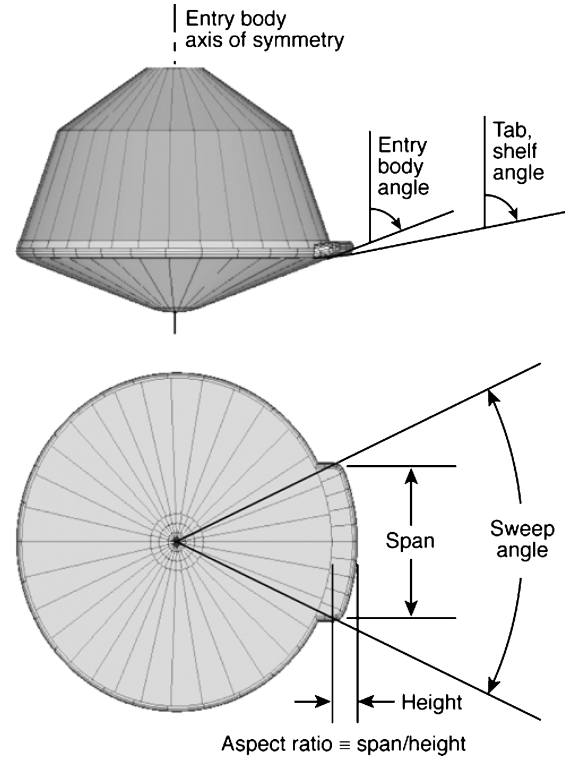


**Fig. 6** Tab, shelf concept schematic and variable definitions.

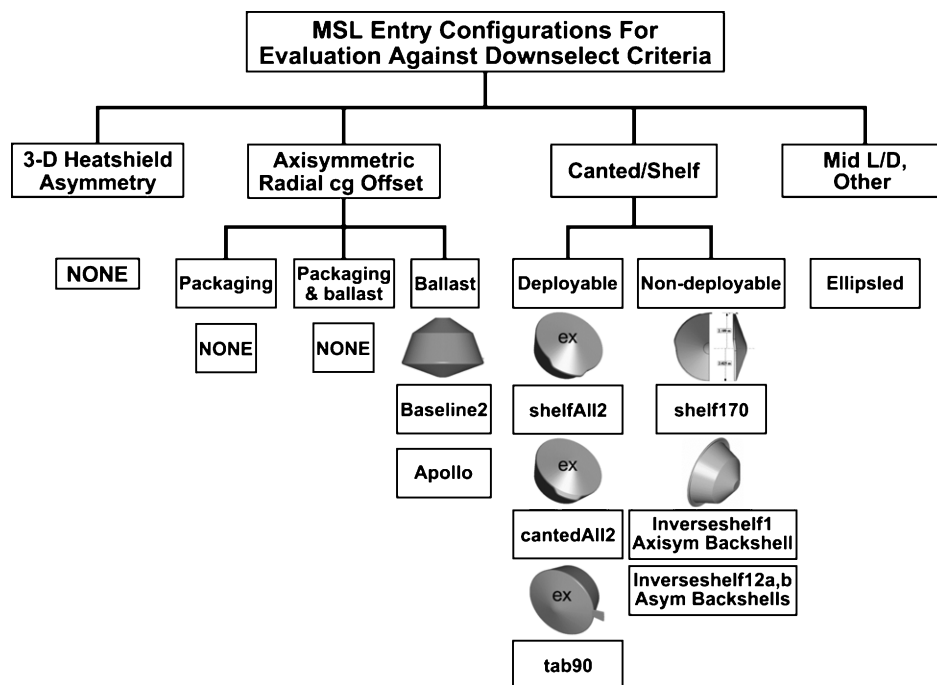


**Fig. 5** Entry body configurations considered for Mars Smart Lander to meet MSR and MSL requirements.



wind-tunnel model for flap 1 is shown in Fig. 7. The effect of the tab on the aerodynamics, as shown in Fig. 7, is to change the trim angle of attack of the entry body. As tab size increases, a slight increase in the  $C_A$  at a given angle of attack results. The  $L/D$  and  $C_N$  as a function of angle of attack are nearly identical for the baseline axisymmetric vehicle and all of the tab sizes tested.

Building from the existing set of data available for the tab concept, variations of the tab were designed for potential MSL configurations using engineering estimates for aerodynamic performance to target an  $L/D = 0.25$ . Concepts were then analyzed with FELISA<sup>8</sup> Euler computational fluid dynamics (CFD) at a given hypersonic Mach number over a range of angle of attack. Based on the CFD results, the configuration was either modified to achieve the target trimmed  $L/D$  or eliminated from consideration as a result of strong shock interactions, large nonlinearities in  $C_{m\alpha}$ , or inadequate performance potential. Configurations were also screened for  $M/C_D S$  and the sensitivity of  $L/D$  to axial c.g. location,  $d(L/D)/d(X_{cg})$ . Several variations of the tab concept were considered, including 90-deg tabs aft of maximum diameter of the vehicle, 90-deg tabs at maximum diameter, 80-deg tabs at maximum diameter, and changes in tab aspect ratio, size, and blending. Tabs could be considered fixed or single time deployable.

Figures 8 and 9 show the hypersonic performance of two concepts, a 90-deg tab at maximum diameter, and an 80-deg canted tab, respectively. The greater the tab angle, the smaller the tab can be to provide the same pitching moment and resultant trim angle of attack. However, the heating is expected to increase with increasing tab angle. Further analysis is therefore required to determine whether there is any significant mass trade for the various concepts.

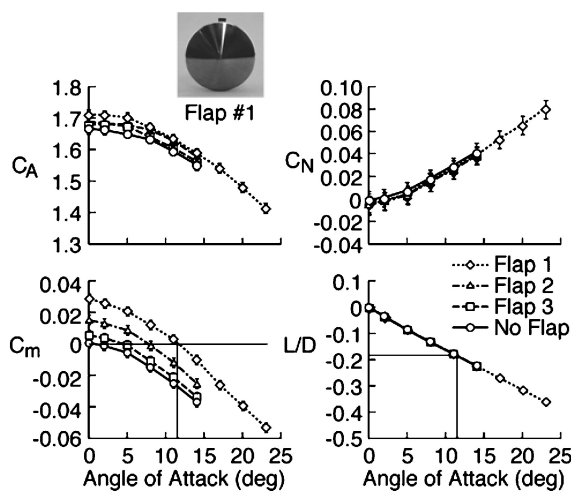


Fig. 7 Flap 1 wind-tunnel model and effect of tab on longitudinal aerodynamic coefficients for MSP '01 precision lander. Results are from LaRC 20 Inch Mach 6 CF4 tunnel.<sup>7</sup>

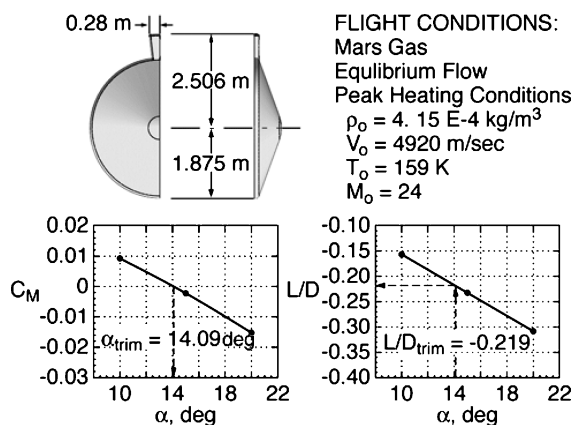


Fig. 8 Ninety-degree tab concept located at maximum diameter (heat shield mounted).

Table 2 Shelf aspect-ratio effect (comparison shown at Mach 24 flight conditions)

Characteristic	Shelf 2	4.05-m shelf
Alpha trim, deg	-14.2	-15
c.g. rad, m	0	0
$L/D$	0.24	0.25
$M/C_D S$ , kg/m <sup>2</sup>	113	115
$d(L/D)/d(c.g. \text{ axial}), \text{ m}^{-1}$	0.030	0.026
Shelf area/S, %	6.2	9.7

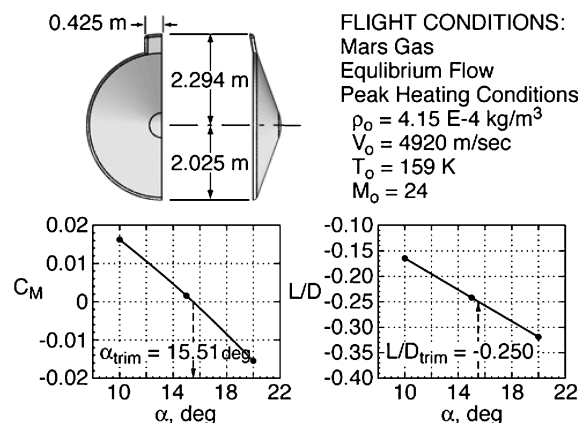


Fig. 9 Eighty-degree canted tab concept.

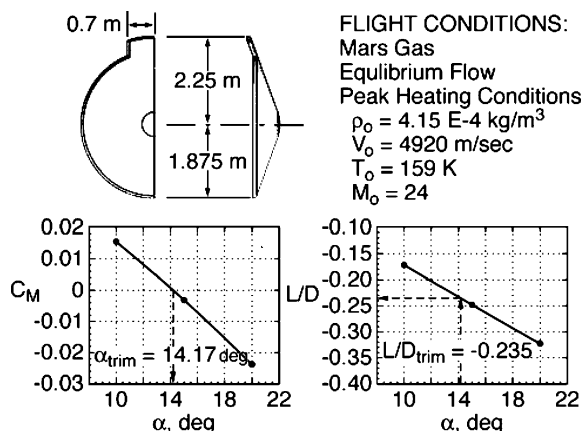


Fig. 10 Shelf2 concept and performance.

The angle of the tab also impacts the trim angle of attack at parachute deploy. The greater the tab angle the lower the trim angle of attack at parachute deploy for a given hypersonic  $L/D$ .

Shelf concepts, defined as tabs at 70 deg to the body centerline, in other words, extensions of the 70-deg sphere cone, were also designed and analyzed. One of the early shelf concepts is shown in Fig. 10. The shelf area must be greater than the tab area for the same  $L/D$ ; however, the shelf is expected to have lower aeroheating, both caused by lack of compression. The shelf aspect ratio can be modified to provide a range of configurations. As the span of the shelf increases, the area of the shelf must increase to provide the same aerodynamic moment. This is because of the reduction in the moment arm as the maximum radius of the shelf decreases and the span increases. Assuming the structural areal density remains the same over the range of shelf aspect ratios considered, the mass penalty, to provide the same  $L/D$ , increases as the shelf span increases. Table 2 illustrates two shelf concepts with similar  $L/D$  performance but with different shelf aspect ratios. Selection

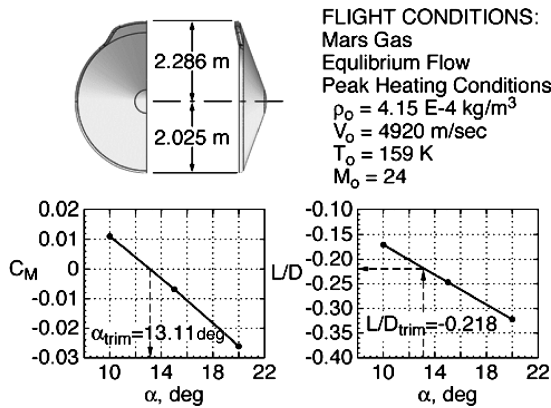


Fig. 11 ShelfAll.

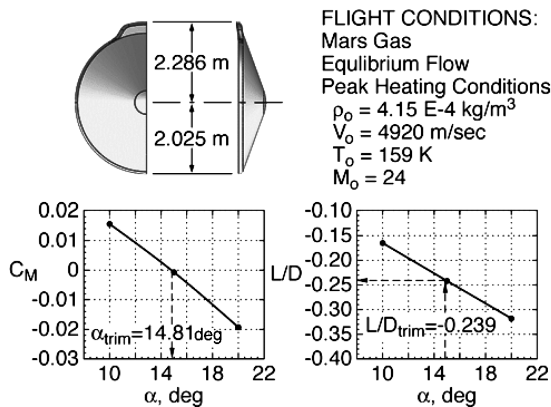


Fig. 12 CantedAll.

of aspect ratio for a particular mission will be dependent on volume considerations within the launch vehicle fairing, or on whether or not the shelf will be stowed during launch and deployed before atmospheric entry or fixed.

The shelf and canted tab concepts were further refined by cross-sectional thickness increases and blending for aeroheating and structural considerations. Figures 11 and 12 show the updated configurations, shelfAll and cantedAll, respectively. The shelfAll, cantedAll, baseline, and derivative of shelf2 configurations were tested in the LaRC Unitary Plan Wind Tunnel for supersonic aerodynamic characteristics.<sup>9</sup> A derivative of shelf2 was also tested in the Ames Research Center ballistic range to assess dynamic stability derivatives of the shelf class of configurations in the supersonic flight regime.<sup>10</sup> The aerodynamic database for the shelfAll configuration is discussed in Ref. 11. Several configurations were tested in the LaRC 20 Inch Mach 6 Air tunnel to assess the aeroheating of the shelf, tab, and baseline geometries.<sup>12,13</sup> Development of the MSL aeroheating environments is discussed in Ref. 14. A performance comparison of the shelfAll and the baseline configuration is discussed later in this paper.

A schematic of an early MSL configuration is shown in Fig. 13, where the entry body diameter was sized for  $M/C_D S$  and the shelf height maximized such that the max radius of the shelf equals the radius of the launch shroud static payload fairing diameter. The aspect ratio of the shelf can also be increased, and the same  $L/D$  performance provided, also shown in Fig. 13. If, instead of defining the entry body for a given payload, the vehicle must maximize payload to the surface such as for MSR, it is desirable to maximize the percent area of the launch-vehicle fairing used by the heat shield. In Fig. 14, the aspect ratio of the shelf can be increased while holding the maximum radius of the shelf equal to the radius of the static payload fairing. As the shelf span increases toward 180 deg, the body diameter increases. The 180-deg shelf has a significant increase in the percent area of the launch-vehicle fairing utilized and a maxi-

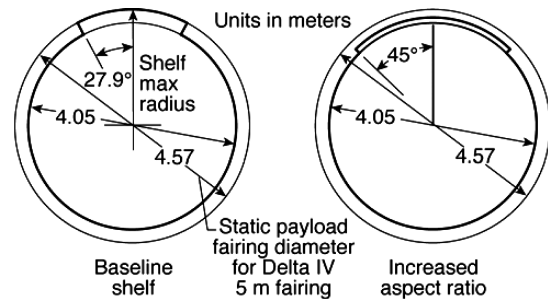


Fig. 13 Shelf concept for Smart Lander in 5-m Delta IV launch-vehicle fairing.

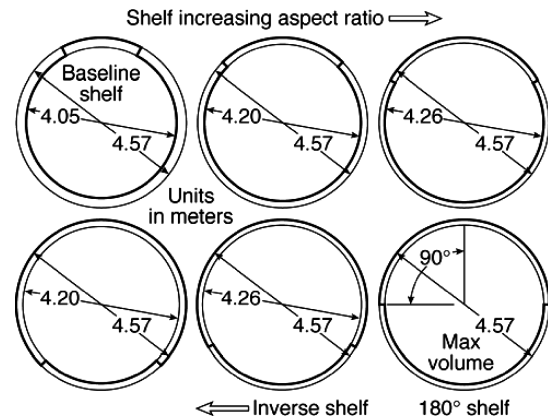


Fig. 14 Shelf aspect-ratio schematic.

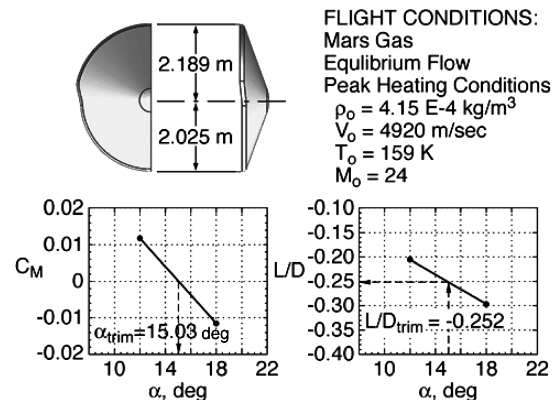


Fig. 15 One-hundred-seventy-degree shelf concept and performance at Mach 24.

imum vehicle body diameter. The maximum vehicle body diameter can be beneficial for MSR packaging. As the shelf wraps farther around the body, from 180 deg to greater than 180 deg, an "inverse shelf" results. The pitching moment of the lee side of the shelf is partially cancelled by the pitching moment created by the wind side of the shelf, resulting in zero net change in the trim  $L/D$ . However, the percent area of the launch-vehicle fairing used by the heat shield continues to increase. Therefore, the inverse shelf fills more of the launch-vehicle-fairing area than the 180-deg shelf providing increased entry mass. Note however that as the shelf wraps around the body from 180 deg to greater than 180 deg, the body diameter decreases. This results in a design with less than the maximum volume available.

Figure 15 shows a realistic version of the 180-deg shelf, with a 170-deg shelf concept blended to 180 deg, and the corresponding hypersonic performance from FELISA CFD results. Figures 16a and 16b show a realistic version of an inverse shelf concept and the corresponding hypersonic performance from FELISA CFD results. Note

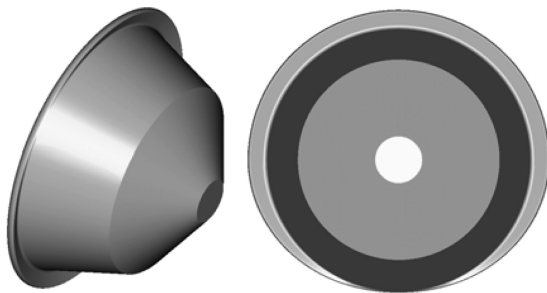


Fig. 16a Inverse shelf concept.

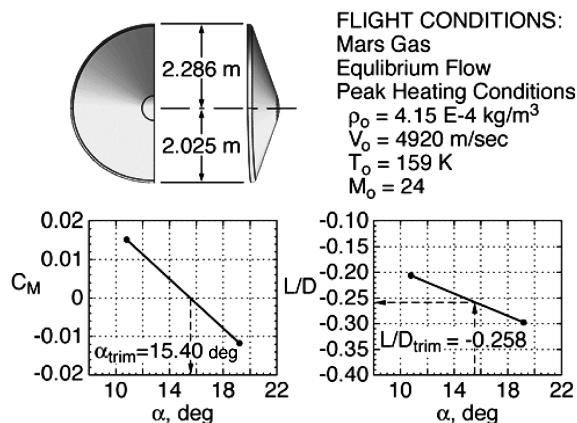


Fig. 16b Inverse shelf performance at Mach 24.

that the corners of the inverse shelf have been blended to the body diameter to reduce the localized aeroheating. Figure 16a shows an inverse shelf concept with an axisymmetric backshell. It is also possible to design a nonaxisymmetric backshell to increase the internal volume of the vehicle. This does result in a backshell mass penalty and adds to the complexity of the design. The volume is also added in the direction opposite to that desirable for radial c.g. offset. In addition it might not be desirable to mate the backshell maximum diameter to the inverse shelf maximum diameter. As the design evolves and the c.g. shifts axially, it would be possible to maintain the vehicle performance, without the addition of ballast, with adjustments in the sizing of the inverse shelf, for example, adjusting the sweep. If the backshell were mated exactly to the inverse shelf maximum diameter, changes to the shape of the heat shield would impact the backshell design and could impact the packaging also.

Another option to be considered to maximize payload to the surface is to use a single time-deployable tab or shelf. This option allows the vehicle body diameter to be equal to the payload static fairing diameter, thus maximizing both the fraction of the launch-vehicle-fairing area used by the heat shield and the vehicle volume available for packaging. However, the concept must be developed, analyzed, and tested. Figure 17 shows an initial mechanical concept for the deployable tab in the launch and deployed configuration. Two sets of four bar linkages hold the tab below the aeroshell for launch and at the deployed position for aeromaneuvering. The wind surface of the deployable concept (not shown) can be shaped for a 90-deg, 80-deg tab, or a 70-deg shelf.

Another option explored to maximize payload to the surface is to use part of the launch-vehicle volume beyond the payload static fairing to accommodate the shelf or tab. The tab or shelf height that could physically extend beyond the payload static fairing is dependent on the particular fairing size and design.

## VI. Low- $L/D$ Configuration Performance Comparisons

Performance comparisons between the shelfAll and the baseline axisymmetric vehicle have been completed using the atmospheric flight simulation presented in Ref. 3 with the baseline aerodynamic database represented in Fig. 4 and the shelfAll aerodynamic database

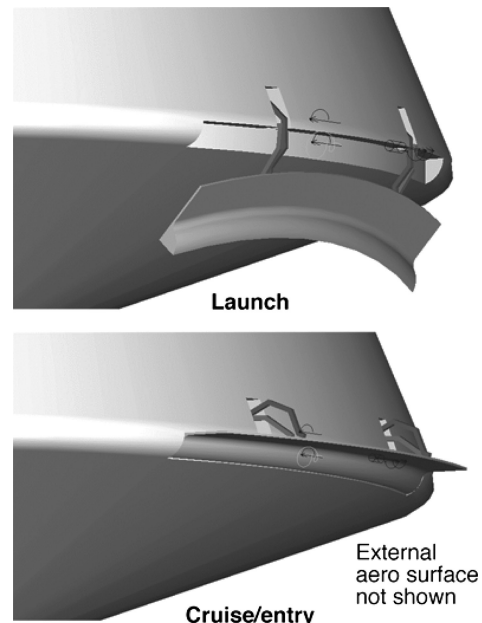


Fig. 17 Deployable tab.

described in Ref. 11. The comparison between the shelfAll and baseline configurations is made for the 27 October 2010 Mars arrival date with a nominal flight-path angle at entry of  $-14.5$  deg. The entry states have delivery errors of  $\pm 0.34$  deg at atmospheric interface, based on radiometric, delta DOR (demonstrated by Odyssey), and optical navigation (planned for demonstration by Mars Reconnaissance Orbiter) for landing at the challenge site at  $41.45\text{S}$ ,  $286.5\text{E}$ . (The entry, descent, and landing challenge site was selected only as a site to challenge the entry, descent, and landing system.) The landing site elevation is  $\sim 2.5$  km above the MOLA geoid. The MarsGram 2001 atmosphere model is used for the above arrival date, dust  $\tau = 0.1$  to  $0.9$ , and  $\text{rpscale} = 1$ . (Dust  $\tau$  affects the mean density profile, and  $\text{rpscale}$  defines the magnitude of the perturbations relative to the mean.) The terminal point controller guidance was used and is discussed in Ref. 15. The vehicle entry mass and body diameter is  $2200$  kg and  $4.05$  m for each vehicle, respectively. The axial c.g. location for each vehicle is  $X_{cg}/D = 0.32$ . ( $X_{cg}$  = axial distance along the centerline measured from the vehicle nose, and  $D$  = vehicle diameter.) The radial c.g. location is zero for the shelfAll configuration. The  $L/D = 0.24$  for the shelfAll configuration at the maximum dynamic pressure along its nominal trajectory. The  $Z_{cg}/D$  for the baseline axisymmetric configuration is defined to result in  $L/D = 0.24$  at the maximum dynamic pressure along its nominal entry trajectory. Two thousand Monte Carlo simulations were completed for each configuration, including dispersions in entry state (delivery and navigation), atmosphere, and aerodynamics, among others.

Figure 18 shows the navigated crossrange vs downrange for the shelfAll configuration at supersonic parachute deploy for 2000 Monte Carlo dispersed cases. Here, 99.7% of the cases have a navigated range of less than  $0.089$  km at supersonic parachute deploy. In other words, the guidance was able to reach the target, converging all of the dispersions, including entry states, atmosphere, and aerodynamics. The result also indicates that the  $L/D = 0.24$  control authority was adequate. Figure 19 shows the actual crossrange vs downrange at supersonic parachute deploy. Here, 99.7% of the cases have an actual range of less than  $6.5$  km. This error is caused by the navigation or knowledge errors originating from the states at atmospheric interface. These errors are unknown to the guidance, and therefore the guidance cannot eliminate them. Figure 20 shows the Mach number vs dynamic pressure at supersonic parachute deploy for the 2000 cases, as well as the Mach, dynamic pressure chute deploy constraint box. To ensure a successful parachute deploy, deploy must occur inside the parachute deploy box. Note that 100%

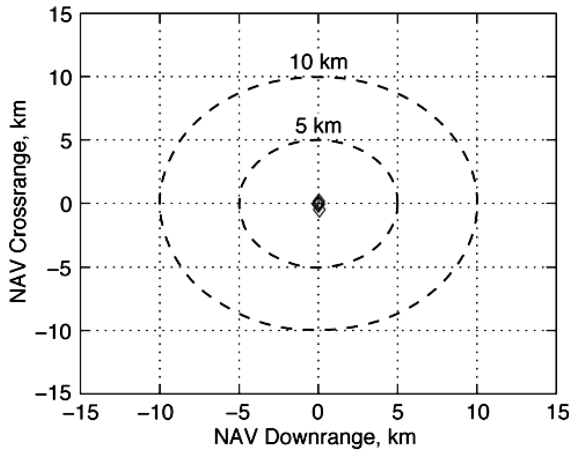


Fig. 18 Target miss distance NAV (state variables calculated by navigation system) minus target at chute deploy for the shelfAll configuration.

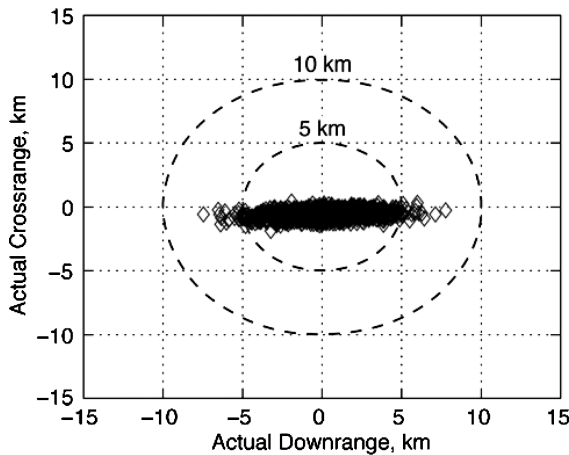


Fig. 19 Target miss distance actual minus target at chute deploy for the shelfAll configuration.

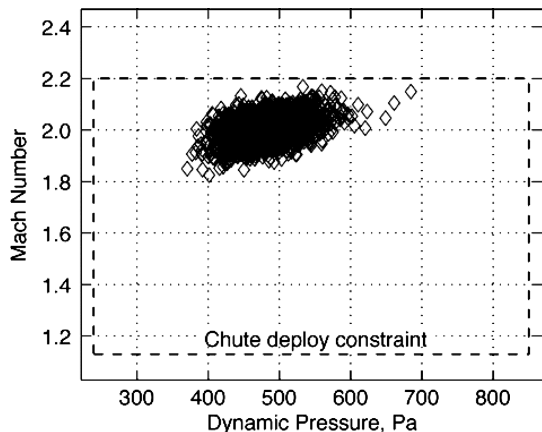


Fig. 20 Mach number vs dynamic pressure at chute deploy for the shelfAll configuration.

of the cases meet the parachute deploy constraints. Figure 21 shows the navigated vs actual altitude at parachute deploy. Note that the navigated altitude, for this particular arrival, is  $\sim 3$  km lower than the actual altitude in the cases with the lowest parachute deploy altitudes. Figures 22 and 23 show the maximum Earth  $g$  during entry, and the stagnation-point heat load vs heat rate for the 0.91-m reference nose radius, for the 2000 cases.

Figures 24–29 show the same plots for the baseline axisymmetric configuration. The baseline configuration results in very similar per-

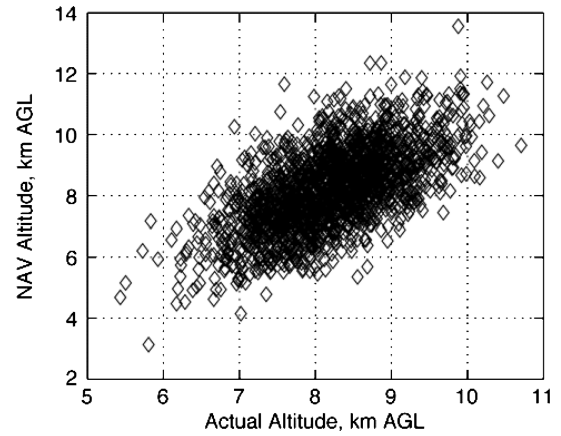


Fig. 21 NAV altitude vs actual altitude at chute deploy for the shelfAll configuration.

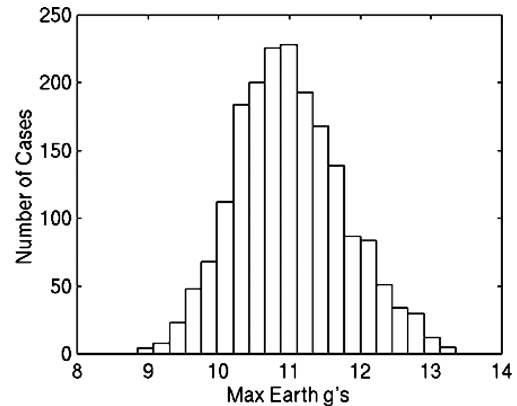


Fig. 22 Number of cases vs maximum Earth  $g$  for the shelfAll configuration.

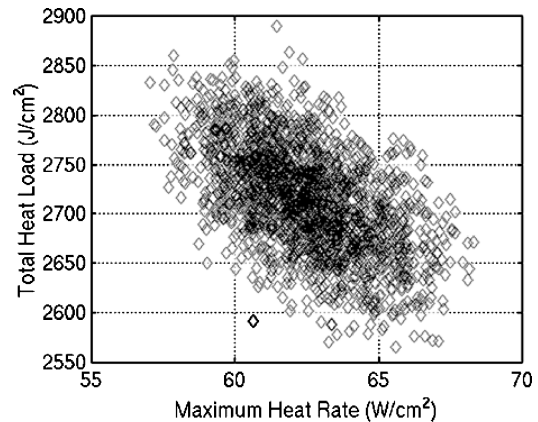


Fig. 23 Stagnation-point total heat load vs maximum heat rate for the shelfAll configuration.

formance as compared to the shelfAll configuration. The primary difference is in the parachute deploy altitude. The ballistic coefficient for the baseline configuration is approximately 6.5% greater than that for the shelfAll configuration. As a result, the parachute deploy altitude is reduced by approximately 0.5 km for the baseline compared to the shelfAll configuration. There is one case in the baseline configuration Monte Carlo cases that deploys the supersonic parachute  $\sim 4$  km from the deploy target in navigated range, shown in Fig. 24. This case is shown in Fig. 27 with the navigated altitude at parachute deploy of  $\sim 2.7$  km and an actual altitude of 5.6 km above the ground. In this case, the vehicle met the parachute deploy constraints, but was forced to deploy before reaching the supersonic deploy target as a result of a navigated altitude guidance

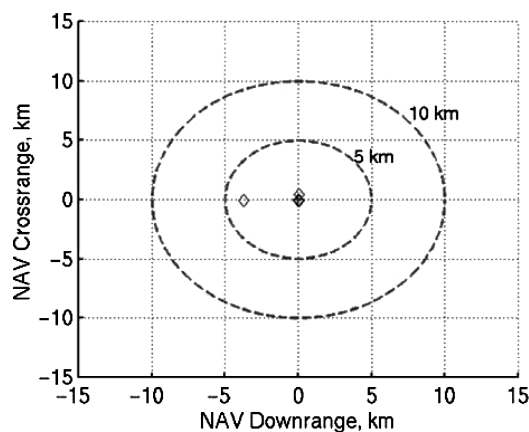


Fig. 24 Target miss distance NAV minus target at chute deploy for the baseline configuration.

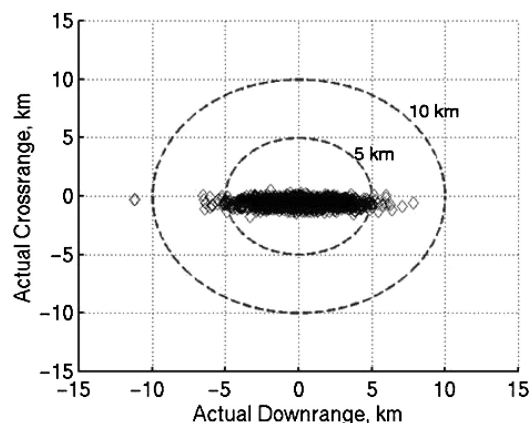


Fig. 25 Target miss distance actual minus target at chute deploy for the baseline configuration.

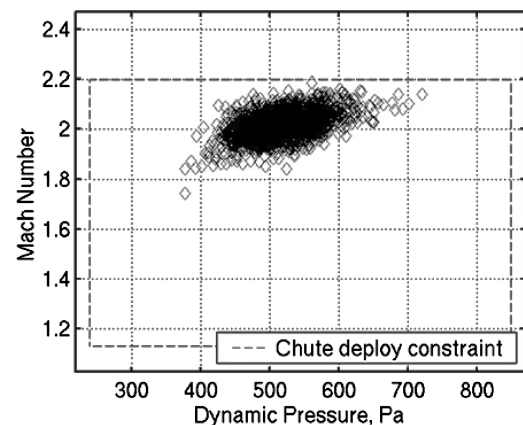


Fig. 26 Mach number vs dynamic pressure at chute deploy for the baseline configuration.

override. As already noted, the override is typically used to ensure that there is adequate altitude at supersonic chute deploy to allow the parachute and powered descent system to land within the touch-down velocity design constraints. However, in this case, because the navigated altitude errors are so significant, the override essentially results in a premature deploy and causes the vehicle to be several kilometers from the deploy target. This target error could be eliminated if a radar altimeter, utilized during the entry phase of the flight to reduce the navigated altitude errors, were added to the system. Alternatively, the override could be eliminated. However, this approach would remove a safety net for extreme cases where an override might be needed.

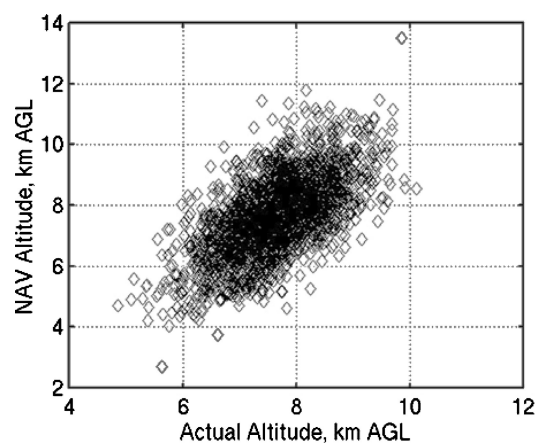


Fig. 27 NAV altitude vs actual altitude at chute deploy for the baseline configuration.

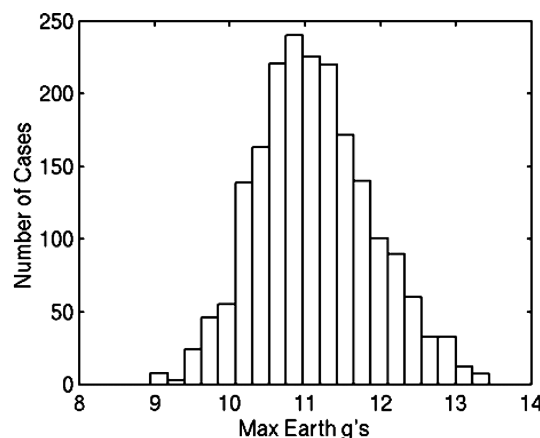


Fig. 28 Number of cases vs maximum Earth  $g$  for the baseline configuration.

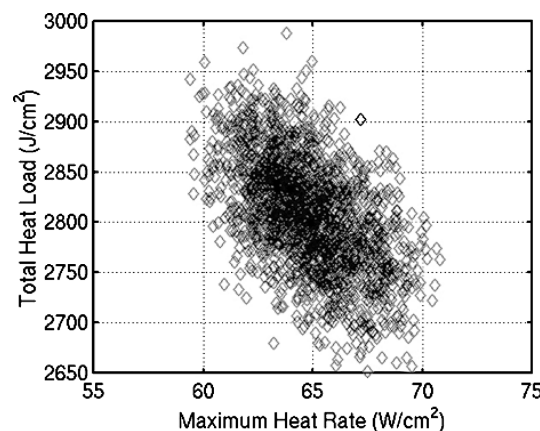


Fig. 29 Stagnation-point total heat load vs maximum heat rate for the baseline configuration.

The preceding comparison is valid for the shelfAll and baseline with the same body diameter. If the requirements drive the body diameter to be equal to the maximum diameter of the launch-vehicle fairing, the comparison would be valid only if the shelf were deployable, or if the shelf could be accommodated beyond the maximum static payload fairing diameter. With the body diameters equal and maximized for the static payload fairing diameter of the 5-m launch fairing, the shelfAll configuration is expected to deliver >200-kg additional payload mass to the Mars surface for MSR-class missions compared to the axisymmetric ballasted 70-deg sphere-cone shape under the same constraints. Each has equivalent internal volume available.

Alternatively, if the requirements drive the body diameter to be equal to the maximum diameter of the launch-vehicle fairing, and the deployable concept or extension beyond the fairing are not options, concepts such as the 180-deg shelf or the inverse shelf can be considered. If mass is not a constraint, or if packaging for a radial c.g. offset is possible, the lowest cost, heritage proven concept is the baseline ballasted axisymmetric shape.

## VII. Mid- $L/D$ Ellipsled Configuration

Another option considered is the mid- $L/D$  slender-body aeroshell called an ellipsled, which is shown in Fig. 30. The front part of the ellipsled is a prolate spheroid extending to a cylinder in the back that results in a configuration with no discontinuities in the slope of the outer surface. This shape originated from studies for human missions to Mars in which large volumes and masses, low load factor constraints, and the desire to avoid on-orbit construction of the aeroshell were the major factors defining the configuration. This vehicle is flown at 55-deg angle of attack, which was selected to minimize the hypersonic ballistic coefficient ( $M/C_D S$ ) while maintaining a high  $L/D$ . The  $L/D$  is a function of the vehicle length-to-diameter ratio ( $l/d$ ) and the angle of attack of the aeroshell. This aeroshell configuration was analyzed for the robotic class of Mars Landers for aeroshells with diameters of 3.75 and 4.572 m selected to fit in the Delta IV 4- and 5-m farings, respectively. The initial length of the 3.75-m ellipsled was selected to fit in a Delta IV 4-m faring giving a  $l/d$  of 1.686. This  $l/d$  was maintained for the 4.572-m ellipsled analysis. Initial detailed analysis was done on the 3.75-m ellipsled and then expanded as needed to the 4.572-m case. The hypersonic lift-and-drag coefficients and the  $L/D$  as a function of angle of attack for  $l/d$  of 1.686 is shown in Fig. 31. A 55-deg angle of attack at supersonic speeds was selected to optimize the  $L/D$  and  $C_D$ . The angle of attack,  $L/D$ ,  $C_L$ , and  $C_D$  are shown as a function of Mach number in Fig. 32.

This configuration, which has no aerodynamic fins or control surfaces, has been shown to be aerodynamically stable for the selected angle of attack, with a center-of-mass location of 52.88% longitudinally and 2.77% laterally. The longitudinal stability characteristics are shown in Fig. 33 for the nominal c.g. location. This graph indicates that the  $C_m$  alpha is stable (negative slope with alpha) throughout the Mach range. These data indicate that the vehicle will trim

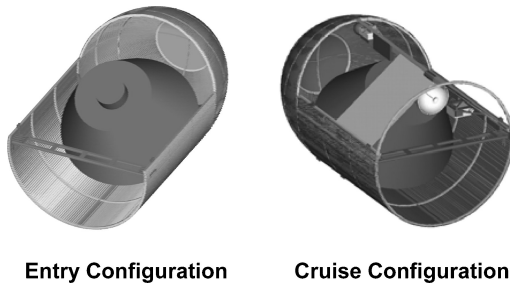


Fig. 30 Ellipsled configurations.

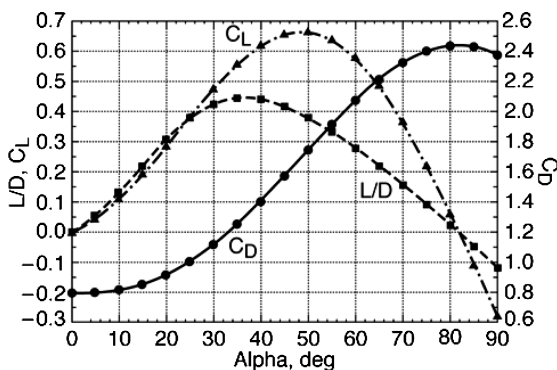


Fig. 31 Characteristic plot of  $C_D$ ,  $C_L$ , and  $L/D$ .

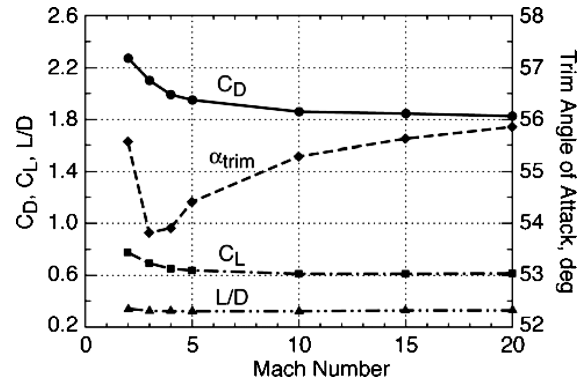


Fig. 32 Navier-Stokes aerodynamic coefficients vs Mach.

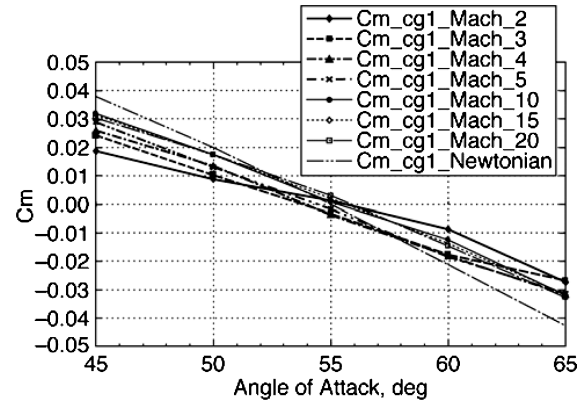


Fig. 33 Navier-Stokes pitching-moment data c.g. at  $X = 52.88\%$ ,  $Z = 2.77\%$ .

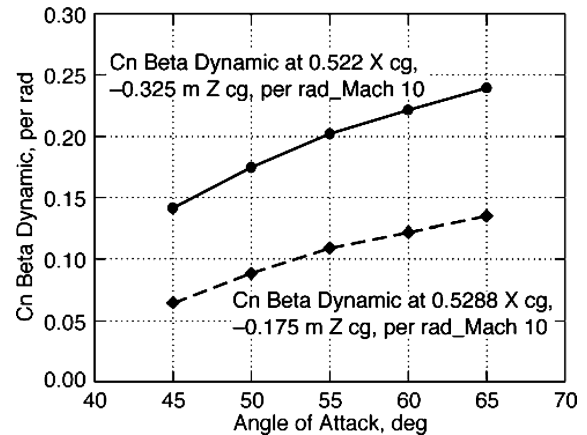


Fig. 34 Effect of  $Z_{cg}$  on  $C_n$  beta dynamic at Mach 10.

within approximately  $\pm 1$  deg of 55-deg angle of attack throughout the Mach range and no longitudinal trim flap should be required. Figure 34 shows the lateral-directional stability characteristics at Mach 10 using the  $C_{n\beta_{\text{dynamic}}}$  parameter for two different  $Z_{cg}$  locations. Increasing the  $Z_{cg}$  offset from  $-0.175$  to  $-0.325$  m almost doubles the  $C_{n\beta_{\text{dynamic}}}$  value and hence the lateral directional stability. Six-degree-of-freedom (DOF) simulations, using a simple flight control system, show that the  $-0.175$ -m offset is adequate for lateral directional control.

Using these aerodynamic properties, the unaugmented stability characteristics were evaluated using closed-form solutions to the equations of motion to define the attitude dynamics. Figure 35 shows the dynamic pressure with the longitudinal short-period frequency characteristics at the trim angle of attack. The lateral-directional stability characteristics are shown in Fig. 36. Also shown in these figures are the Mil-Spec 8785C flying quality requirements that

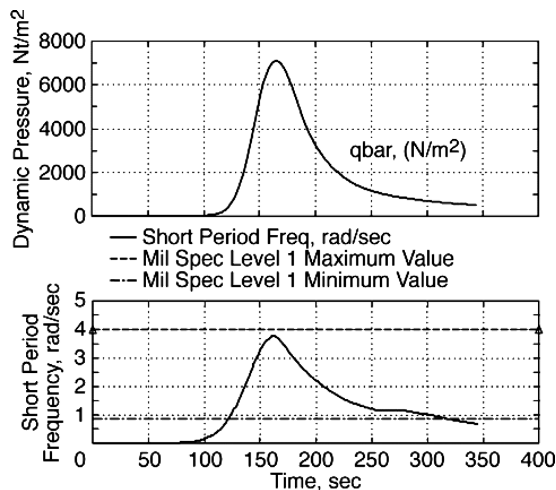


Fig. 35 Dynamic pressure and pitch-axis short-period frequency compared with Mil Spec 8785C approximate level 1 flying quality values: c.g. at  $X = 52.88\%$ .

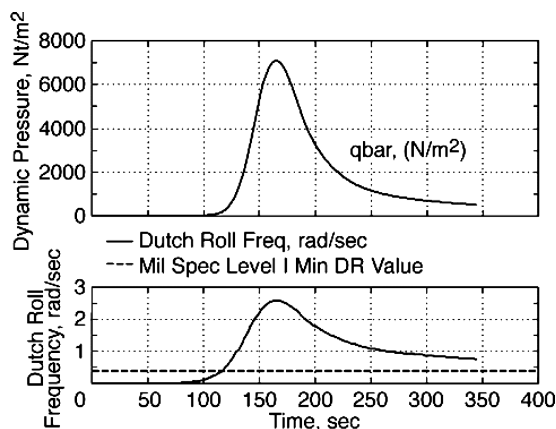


Fig. 36 Dynamic pressure and Dutch roll frequency compared with Mil Spec 8785C approximate level 1 flying qualities: c.g. at  $X = 0.5288\%$ .

provide a reasonable approximation for evaluating the unaugmented stability characteristics. These figures show that the unaugmented vehicle meets the Mil Spec requirements except at the beginning and the end of the flight when the dynamic pressure is very low and the RCS easily provides the torque needed to provide the necessary stability characteristics. A six-DOF simulation analysis with a simple attitude control feedback system has shown that a RCS system provides sufficient stability and control throughout the entry flight.

The RCS system used in the six-DOF simulations assumed a hydrazine blowdown system with three up-, three down-, and three side-firing jets on each side at the back of the ellipsoid. Using this RCS system, a flight control system that provided adequate control for the vehicle for nominal and dispersed cases including c.g. uncertainties and aerodynamic uncertainties was designed. Propellant requirements were minimized by the use of control deadbands about the natural vehicle trim angles. Figures 37 and 38 show the simulation results with a  $Y_{cg}$  offset of 2.54 cm for the bank-angle control profile and the resulting sideslip angle. These results indicate that the flight control system can control the vehicle with this large  $Y_{cg}$  offset but with a sideslip angle of 6 to 7 deg, a reorientation of the lift vector with respect to the aeroshell body of about 10 deg, and an increase in the RCS propellant by a factor of about 2.5. The structural design of the cylindrical part of the ellipsoid is rolled up 10 deg on both sides to account for the potential sideslip associated with this size  $Y_{cg}$  offset. The 2.54-cm  $Y_{cg}$  offset is considered a reasonable constraint for this configuration based on these results. Additional simulations were done with aerodynamic uncertainties of 0.001 and 0.0005 in both the rolling-moment coefficients and yawing-moment coefficients. The simulation was completely ade-

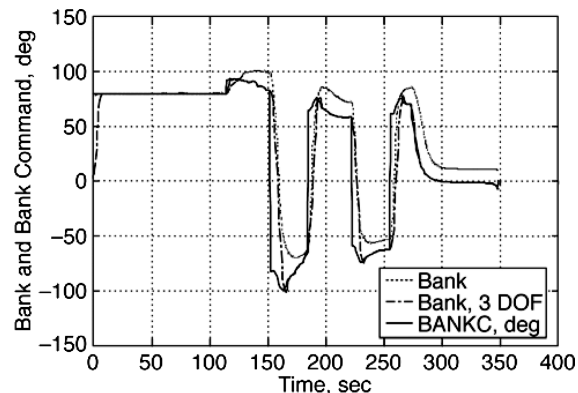


Fig. 37 Bank angle for 2.54-cm  $Y_{cg}$  offset compared with nominal three-DOF bank and bank command.

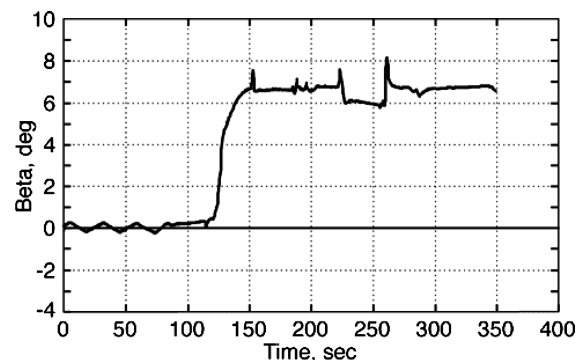


Fig. 38 Sideslip angle for 2.54-cm  $Y_{cg}$  offset.

quate for these cases, and it was determined that a propellant load of 31 kg of hydrazine would be sufficient for reasonable dispersions for the 3.75-m-diam ellipsoid. The propellant load for the larger 4.572-m-diam ellipsoid is 71 kg.

Performance analysis of the mid- $L/D$  ellipsoid configuration for robotic class Mars Landers has shown that the relatively large  $L/D$  and corresponding  $m/C_D S$  results in the capability to fly larger masses to the parachute deployment constraint envelope compared to the low- $L/D$  aeroshell configurations. However, structural analysis has shown that considerably more launch mass is required for this configuration. Preliminary analysis indicates that the ellipsoid configuration is capable of landing 15 to 20% more mass on the surface compared to a low- $L/D$  aeroshell of the same diameter for the same parachute envelope constraints but at a cost of 40 to 50% launch mass. It also has more volume available for packaging of the payload.

The ellipsoid configuration has not been certified for any atmospheric mission and thus would require extensive and expensive testing and qualification before it would be selected for a Mars mission. These facts and the desire to fly the first precision landing mission with a known configuration eliminated the ellipsoid from consideration for the MSL mission. Interest for possible future Mars robotic missions however led to a cost assessment of the mid- $L/D$  aeroshell and high Mach parachute for the Mars Program Systems Engineering Team performed by the NASA Aeroassist Working Group.

## VIII. Conclusions

Several configurations have been identified and analyzed as alternatives to the 70-deg axisymmetric ballasted sphere cone. Among the configurations, several are expected to deliver >200-kg additional landed mass to the Mars surface for MSR-class missions compared to the axisymmetric ballasted 70-deg sphere-cone shape under the same constraints. With the available database, configurations can be readily selected and tailored to meet a particular set of project requirements.

## Acknowledgments

The authors recognize the contributions of the Mars Smart Lander entry, descent, and landing team members at Jet Propulsion Laboratory, NASA Johnson Space Center, ARC, and NASA Langley Research Center (LaRC). In addition, the following are special thanks to individuals without whose efforts this paper would not have been possible. Thank you to M. Schoenenberger and F. M. Cheatwood, NASA LaRC, for their configuration work. Thank you to Steve Hughes and John Teter, NASA LaRC, for the deployable tab mechanical concept. Thank you to Scott Striepe, NASA LaRC, for the Monte Carlo analysis results. Thank you to M. L. McMillin, NASA LaRC, for the tab geometry. Thank you to T. J. Horvath, LaRC, for the LaRC Mach 6 CF4 data on the tab configurations proposed for the Mars Surveyor 2001 Precision Lander. Thank you to Anne Rhodes for preparing this document.

## References

- <sup>1</sup>Carman, G. L., Ives, D. G., and Geller, D. K., "Apollo-Derived Precision Lander Guidance," AIAA Paper 98-4570, Aug. 1998.
- <sup>2</sup>Striepe, S. A., Queen, E. M., Powell, R. W., Braun, R. D., Cheatwood, F. N., Aguirre, J. T., Sachi, L. A., and Lyons, D. T., "An Atmospheric Guidance Algorithm Testbed for the Mars Surveyor Program 2001 Orbiter and Lander," AIAA Paper 98-4569, Aug. 1998.
- <sup>3</sup>Striepe, S. A., Way, D. W., Dwyer, A. M., and Balaram, J., "Mars Science Laboratory Simulations for Entry, Descent, and Landing," *Journal of Spacecraft and Rockets*, Vol. 43, No. 2, 2006, pp. 311–323.
- <sup>4</sup>Lockwood, M. K., Powell, R. W., Graves, C. A., and Carman, G. L., "Entry System Design Considerations for Mars Landers," AAS Paper 01-023, Jan. 2001.
- <sup>5</sup>Calhoun, P. C., and Queen, E. M., "Entry Vehicle Control System Design for the Mars Science Laboratory," *Journal of Spacecraft and Rockets*, Vol. 43, No. 2, 2006, pp. 324–329.
- <sup>6</sup>Sammonds, R. I., and Dickey, R. R., "Effectiveness of Several Control Arrangements on a Mercury-Type Capsule," NASA TM X-579, Oct. 1961.
- <sup>7</sup>Horvath, T. J., O'Connell, T. F., Cheatwood, F. M., Prabhu, R. K., and Alter, S. J., "Experimental Hypersonic Aerodynamic Characteristics of Mars Surveyor 2001 Precision Lander with Flap," *Journal of Spacecraft and Rockets*, Vol. 43, No. 2, 2006, pp. 270–281.
- <sup>8</sup>Peiro, J., Peraire, J., and Morgan, K., "FELISA System Reference Manual and Users Guide," NASA CP-3291, May 1995.
- <sup>9</sup>Murphy, K. J., Horvath, T. J., Erickson, G. E., and Green, J. M., "Supersonic Aerodynamic Characteristics of Proposed Mars '07 Smart Lander Configurations," *Journal of Spacecraft and Rockets*, Vol. 43, No. 2, 2006, pp. 282–292.
- <sup>10</sup>Brown, J., Yates, L., Bogdanoff, D., Chapman, G., Loomis, M., and Tam, T., "Free-Flight Testing in Support of the Mars Science Laboratory Aerodynamics Database," *Journal of Spacecraft and Rockets*, Vol. 43, No. 2, 2006, pp. 293–302.
- <sup>11</sup>Bobskill, G. J., Parikh, P. C., Prabhu, R. K., and Tyler, E. D., "Aerodynamic Database Development for Mars Smart Lander Vehicle Configurations," *Journal of Spacecraft and Rockets*, Vol. 43, No. 2, 2006, pp. 303–310.
- <sup>12</sup>Liechty, D. S., Hollis, B. R., and Edquist, K. T., "Mars Science Laboratory Experimental Aerothermodynamics with Effects of Cavities and Control Surfaces," *Journal of Spacecraft and Rockets*, Vol. 43, No. 2, 2006, pp. 340–353.
- <sup>13</sup>Hollis, B. R., and Liechty, D. S., "Transition Due to Heat-Shield Cavities on a Mars Entry Vehicle," *Journal of Spacecraft and Rockets*, Vol. 43, No. 2, 2006, pp. 354–366.
- <sup>14</sup>Edquist, K. T., Liechty, D. S., Hollis, B. R., Alter, S. J., and Loomis, M. P., "Aeroheating Environments for a Mars Smart Lander," *Journal of Spacecraft and Rockets*, Vol. 43, No. 2, 2006, pp. 330–399.
- <sup>15</sup>Mendeck, G. F., and Carman, G. L., "Guidance Design for Mars Smart Lander Using the Entry Terminal Point Controller," AIAA Paper 2002-4502, Aug. 2002.

M. K. Lockwood  
Guest Editor